Mechanical Technology and Engineering Insights

www.mtei.reapress.com

Mech. Technol. Eng. Insights. Vol. 3, No. 2 (2026) 81–100.

Paper Type: Original Article

Pore-Scale Multiphase MRT-LBM Investigation of Liquid-Water Transport and Injection Location Effects in Compressed Porous Transport Layers of Interdigitated PEM Fuel Cells

Hamid Reza Ashorynejad[1,*], Kourosh Javaherdeh[1]

[1] Department of Industrial, Mechanical and Aerospace Engineering, Buein Zahra Technical University, Buein Zahra, Qazvin, Iran; h.r.ashorynezhad@gmail.com.

[2] Department of Mechanical Engineering, University of Guilan, Rasht, Iran; javaherdeh@guilan.ac.ir.

Citation:

Received: 12 November 2025 *Revised: 01 February 2026* *Accepted: 14 April 2026*	Ashorynejad, H. R., & Javaherdeh, K. (2026). Pore-scale multiphase MRT-LBM investigation of liquid-water transport and injection location effects in compressed porous transport layers of interdigitated PEM fuel cells. *Mechanical Technology and Engineering Insights*, *3*(2), 81-100.

Abstract

The transport of liquid water is crucial in water management in Proton Exchange Membrane Fuel Cell (PEMFCs) since the presence of too much liquid water in Porous Transport Layers (PTLs) may block gas transport and cause flooding in the interdigitated cell structure. This study develops a pore-scale Lattice Boltzmann Model (LBM) for liquid water transport in compressed porous media of interdigitated PEMFCs using the Shan-Chen pseudopotential method and the Multiple-Relaxation-Time (MRT) collision operator. The developed model is first validated against Laplace's law, droplet contact angle, and correlations for permeability for single-phase flow in the PTL. The results of the validated model are used to analyze the impact of liquid water injection location on water saturation and drainage. The water is injected into three different locations: beneath the gas inlet, beneath the middle rib region, and beneath the gas outlet. The results show that water saturation and drainage are highly dependent on the water injection location. The highest average water saturation (0.34–0.35) was achieved in the case of inlet-side injection, while the lowest average water saturation (0.12–0.15) was observed when water was injected on the outlet side.

Keywords: Proton exchange membrane fuel cell, Porous transport layer, Liquid-water transport, Water saturation, Multiphase flow, Multiple-relaxation-time lattice Boltzmann method, Pore-scale simulation, Water management.

1 | Introduction

Proton Exchange Membrane Fuel Cells (PEMFCs) have gained popularity in recent decades as an alternative energy source for several applications, including providing traction power in FCEVs (fuel cell electric vehicles)

Corresponding Author: h.r.ashorynezhad@gmail.com

https://doi.org/10.48313/mtei.v3i2.82

Licensee System Analytics. This article is an open access article distributed under the terms and conditions of the Creative Commons Attribution (CC BY) license (http://creativecommons.org/licenses/by/4.0).

[1], [2]. Some of the major benefits of the PEMFC include low operating temperature, high power density, high efficiency, less noise, and lower pollution [3]. Gas Diffusion Layer (GDL) of the PEMFC, which is made up of porous materials such as carbon fibers, facilitates mass transfer and conductance in the CL (catalyst layer) [4]. The compression force exerted on the GDL does not destroy carbon fibers and does not reduce their volume but only reduces the pore space. Moreover, porosity beneath the rib is reduced due to the compression force. Hence, the compression force alters its diffusivity and conductivity [1]. For the cell to achieve optimal performance, it must be able to remove water droplets formed in the CL from the GDL. Compression and deformation of the GDL play a significant role in the ejection of droplets from the GDL and control of water in the GDL [5].

However, it should be taken into consideration that, when the produced water is not removed at a proper rate from the electrode, it will accumulate in the form of a water film that fills up the pores in GDL and leads to flooding, making the transportation of reactants difficult [6], [7]. Several measures have been taken to mitigate the flooding problem by increasing the hydrophobicity of GDL and CL through the introduction of highly hydrophobic material such as Polytetrafluoroethylene (PTFE), insertion of Microporous Layer (MPL) between GDL and CL, and advanced designs of the flow field [3].

One of the famous and efficient flow fields that has been introduced is the interdigitated flow field introduced by Nguyen [8]. In this flow field, the creation of the in-plane pressure gradient in the GDL causes the gas to flow in-plane under the land. This flow helps in the transportation of the reactants' supplies towards the reactive sites, and also the transport of the water through the alternate mechanism from the diffusion to the forced convection in the GDL; consequently, this flow field has solved the flooding problem at the cathode site. As a result, the interdigitated flow field increases the performance of the PEMFC in comparison to the parallel flow field [9–13].

The performance of the interdigitated PEMFCs has been investigated by several studies using different physical parameters. The first parameter under consideration is the influence of the GDL compression. Different studies have been performed in this respect. For instance, Su et al. [14] performed a numerical simulation to investigate the influence of the compression forces on the PEMFC performance. They tested the performance of three different types of GDL and concluded that in the case of non-homogeneous GDL, there would be a marked improvement in the predicted cell performance. By means of numerical simulation, Shin and Wang [15] demonstrated that the influence of the compression forces would become significant in the high current density region. It was found that in the case of ignoring the assembly compression, there would be an overprediction of the fuel cell performance.

Lin et al. [16] investigated the Effect of compaction on two types of GDL fuel cells. The results showed that in the high compression region, the performance and the limiting current of the fuel cell decreased and accordingly, an optimal value for the fuel cell performance was determined. Chipper et al. [17] indicated that the non-uniform compression of the GDL and intrusion of the GDL layer would significantly influence the increase in the degree of non-uniformity in the liquid saturation, the oxygen concentration, and current density distribution. By means of the Lattice Boltzmann Method (LBM), Molaeimanesh and Nazemian [18] proved that the application of compression leads to poorer oxygen distribution and more water vapor accommodation near the catalyst layer surface. Moreover, they obtained the optimal value for the compression ratio for the maximum average current density. Ramiar et al. [19] investigated the effects of the inhomogeneous GDL compression on the performance of PEMFC with an interdigitated flow field. All of the above-mentioned efforts indicate that increasing the compression from 10% to 35% leads to an increase in the flooding of GDL, limited transfer of reactants, and a decrease in the efficiency of the PEMFC.

Shi et al. [20] investigated the Effect of the GDL deformation. It was found that the GDL deformation causes lower oxygen concentration at the reaction sites and an increase in the saturated liquid water level along the flow direction.

Ihonan et al. [21] examined the effects of four commercial GDL materials. They concluded that increasing the clamping pressure leads to flooding of the fuel cell because of the reduction in porosity and the

temperature gradient between the GDL and the current collector. In this study, the presence of water is assumed to be a continuous liquid. In contrast, the continuous movement of liquid water through the pores of the GDL structure is not reported as an in situ observation. On the contrary, the environmental scanning electron microscope observations show that there are small water droplets that exist within the fibrous structure of GDL [22], [23].

LBM can be considered a strong numerical method that enables one to simulate pore-scale multiphase flows such as flow in porous media as well as mass transport in the real structures of GDL [24], [25]. There are many studies that have been done concerning the application of the LBM method in the investigation of liquid water and the transfer process of reactants and the structure of GDL [26–31].

Hao and Cheng [31] analyzed the Effect of GDL wettability on liquid water transport in GDL. The results obtained in this study showed that the employment of hydrophilic passages leads to the improvement in the removal of liquid water from the GDL. As a result, it reduces the possibility of flooding in the GDL and CL. Li Chen et al. [32] studied the Effect of land width and GDL contact angle on the liquid water removal time and found that the narrower land reduces the liquid water removal time. Higher contact angle enhances the removal and decreases the residual saturation.

Kim et al. [30] investigated the liquid water transfer taking into account the MPL and GDL. The authors concluded that there was a reduction in the liquid content of PTL when applying a thicker MPL and/or increasing the hydrophobicity of the solid surface. Molaeimanesh et al. [33] analyzed the Effect of GDL compression on liquid water removal. It was revealed that in the case of hydrophobic GDLs, the Effect of increased compression on the removal process does not depend on the compression amount. On the other hand, compression may not always be effective for hydrophilic GDLs.

Deng et al. [34] applied the LBM method to study the Effect of GDL compression on liquid water removal in PEMFC with an interdigitated flow field. It was found that there is an optimal level of compression for the enhanced liquid water removal. Deng et al. [34] examined the Effect of the way of contact angle definition, PTFE distribution, and pressure difference at the interface of gas diffusion and MPL s. It was found that for the sample of GDL that dried under vacuum conditions, the PTFE distribution inside the whole GDL is almost uniform, thus requiring less time to overcome the water barrier.

The primary objective of the current research work is to examine the effect of liquid-water injection location on pore-scale water transport, drainage process, and water saturation in compressed Porous Transport Layers (PTLs) of an interdigitated PEMFCs. In order to accomplish the above-mentioned objective, a pore-scale multiphase MRT-LBM based on the Shan-Chen pseudopotential approach is established for the simulation of gas and liquid transport in the PTLs.

Initially, the validity of the proposed numerical model is proved by comparing the results of the model with Laplace's law, droplet contact angle behavior, and existing correlations of the single-phase flow through porous media, showing that the model can precisely describe the physical mechanism of the process. Then, after validation of the model, the effects of three representative liquid-water injection locations, such as under the gas inlet, under the rib region, and under the gas outlet, on the liquid-water transport, drainage properties, and water saturation time evolution are examined using the validated model.

2 | Numerical Method

In this paper, Shan and Chen's multicomponent multiphase LBM with Multi-Relaxation Scheme (MRT) is adopted because of its high stability and accuracy compared to that of the single relaxation scheme. Furthermore, a pseudopotential function is applied to simulate the interparticle interaction in lattice Boltzmann. Considering the component k, the collision operator for multicomponent multiphase flows in a 2D lattice can be written as follows:

$$f_a^{\,k}(x + e_a\Delta t, t + \Delta t) - f^k{}_a(x,t) = -\Omega\left[f^k{}_a(x,t) - f_a^{\,k,eq}(x,t)\right] + \Delta t S^k{}_a(x,t), \quad \textbf{(1)}$$

where f_a^k is the Density Distribution Function (DDF), $f_a^{k,}$ eq is its equilibrium distribution for component k, Ω is the collision matrix, t is the time, x is the spatial position, Δt is the time step, $S^k{}_a$ is the forcing term in the velocity space. e_a is the discrete velocity along the ath direction; for D2Q9, ea is defined as follows:

$$e_a = \begin{cases} 0 & a = 0, \\ \left(\cos\left[\frac{(a-1)\pi}{4}\right], \sin\left[\frac{(a-1)\pi}{4}\right]\right) & a = 1,2,3,4. \\ \sqrt{2}\left(\cos\left[\frac{(a-1)\pi}{4}\right], \sin\left[\frac{(a-1)\pi}{4}\right]\right) & a = 5,6,7,8. \end{cases} \quad (2)$$

The MRT shames offer higher stability, accuracy, low spurious velocity, and achievable density ratio [35–37]. *Eq. (1)* by the MRT method can be transformed to the following form:

$$m^{*,k} = m^k - \Lambda\left[m^k(x,t) - m^{k,eq}(x,t)\right]\Big| + \Delta t(I - 0.5\Lambda)F^k{}_m, \quad (3)$$

where $m^k(x,t)$ and $m^{k,eq}(x,t)$ are vectors of moments and the equilibrium vectors of moments for component k, respectively. M is the transformation matrix. A linear transformation can perform the mapping between velocity and moment spaces.

$$m^k = Mf^k, f^k = M^{-1}m^k. \quad (4)$$

For the D2Q9 lattice, the equilibria m^k and $m^{k,\,eq}$ can be written as

$$m^k = \left(\rho, e, \varepsilon, j_x, q_x, j_y, q_y, p_{xx}, p_{yy}\right)^T. \quad (5)$$

$$m^{k,eq} = \rho(1, -2 + 3({u_k}^2 + {v_k}^2), 1 - 3({u_k}^2 + {v_k}^2), u_k, -u_k, v, -v, u^2 - v^2, uv)^T. \quad (6)$$

Λ is the relaxation matrix and is diagonal in momentum space:

$$\begin{aligned} \Lambda &= \mathrm{diag}(S_1, S_2, S_3, S_4, S_5, S_6, S_7, S_8, S_9) \\ &= \mathrm{diag}\left(\tau_\rho{}^{-1} \quad \tau_e{}^{-1} \quad \tau_\varsigma{}^{-1} \quad \tau_j{}^{-1} \quad \tau_q{}^{-1} \quad \tau_j{}^{-1} \quad \tau_q{}^{-1} \quad \tau^{-1} \quad \tau^{-1}\right), \end{aligned} \quad (7)$$

where S_1, S_4, and S_6 should be equal to each other and are considered to be one. S_5 and S_7 equal 1.1, and S_2=S_3 and S_8 = S_9 are related to the bulk and kinematic viscosity, respectively:

$$\lambda = \left(\frac{1}{S_2} - 0.5\right){C_s}^2. \quad (8)$$

$$\nu = (\tau - 0.5)C_s^2, \quad (9)$$

where $C_s = 1/\sqrt{3}$ is the lattice sound velocity, and $\tau = \frac{1}{S_8}$; also, I is the unit tensor, and $(I - 0.5\Lambda)F_m^k$ is the force term in momentum space.

Since in the MRT method the relaxation time is related to the kinematic viscosity, and at a temperature ratio of $\frac{T}{Tc} = 0.5$, the gas-to-liquid dynamic viscosity ratio is about 25, we set relaxation time τ_g to 1.0 for the gas phase, The relaxation time for the liquid phase is calculated using the ratio of kinematic viscosity.

To implement the external force into the LB framework, Gue's method, proposed by Gue et al. [38] is incorporated. McCracken et al. [37], which is claimed to be derived directly from the Boltzmann equation. In this scheme, the force term in the MRT model is derived as follows:

$$F^k{}_m = \left[0, 6(uF^k{}_x + vF_y{}^k), -6(uF^k{}_x + vF^k{}_y), F^k{}_x, -F^k{}_x, F^k{}_y, -F^k{}_y, 2(uF_x{}^k - vF^k{}_y), 2(uF^k{}_x - vF^k{}_y)\right]^T. \quad (10)$$

In this model, the density of the component and velocity can be expressed as follows [38]:

$$\rho^k = \sum_a f_a. \quad (11)$$

$$V^k = \frac{\sum_k \left(\sum_a f_a e_a + \Delta t \frac{F}{2}\right)}{\sum_k \rho^k}, \quad (12)$$

where $F = (F_x, F_y)$ is the total interaction force acting on the component and is expressed as:

$$F^k = F^k{}_{coh} + F^k{}_{adh}, \quad (13)$$

where $F^k{}_{coh}$ is the fluid-fluid interaction force and is defined in the following:

$$F^k coh = F^{kk} + F^{kj}, \quad (14)$$

where F^{kk} is the intra-molecular interaction force and can be written as:

$$F^{kk} = -G_{kk}\psi^k(x) C_s{}^2 \sum w(|e_\alpha|^2)\psi^k(x + e_\alpha)e_\alpha. \quad (15)$$

In which $\psi^k(x)$ is the interaction potential, G_{kk} is the interaction strength, and $w(|e_\alpha|^2)$ are the weights only depending on the length of the vector e_α. The weights are set as w(1) = 1/3 and w(2) =1/12 for the nearest-neighbor interactions on the D2Q9 lattice [39].

The F^{kj} is the interaction force between two components and is written as [40]:

$$F_{12} = -G_{12}\phi_1(x) \sum_{a=1}^{8} w(|e_\alpha|^2)\phi_2(x + e_\alpha)e_\alpha. \quad (16)$$

$$F_{21} = -G_{21}\phi_2(x) \sum_{a=1}^{8} w(|e_\alpha|^2)\phi_1(x + e_\alpha)e_\alpha, \quad (17)$$

where $\phi_1(x)$ and $\phi_2(x)$ are different from $\psi^k(x)$ and are expressed as:

$$\phi_1(\rho_2) = 1 - \exp\left(\frac{-\rho_2}{\rho_{20}}\right). \quad (18)$$

$$\phi_2(\rho_1) = a_0 - \exp\left(\frac{-\rho_1}{\rho_{10}}\right). \quad (19)$$

The values of ρ_{10},ρ_{20},a_0, G_{12} and G_{21} are critical for a multicomponent multiphase system [40–43]; the higher value of which leads to limiting the magnitude of the mutual diffusivity in the gas phase.

In this paper we set $a_0 = 0.005$, $\rho_{10} = \frac{-0.0008}{\log(a_0)}$,$\rho_{20} = 0.0003$ [44], and $G_{12} = G_{21} = 0.0001$.

$F^k{}_{adh}$ is the fluid-solid adhesion force and is calculated by the following equation:

$$F^k{}_{adh}(x) = -G^k{}_{adh}\psi^k(x) \sum w(|e_\alpha|^2)S(x + e_\alpha \Delta t)e_\alpha. \quad (20)$$

In which $G^k{}_{adh}$ is the adhesion factor that determines the strength of the fluid-solid interaction for component k, S is equal to 1 and 0 for solid and fluid domain nodes, respectively.

Component 1 is water and component 2 is air. Air is considered an ideal fluid; thus, $G_{22} = 0$. Water is considered a non-ideal fluid that follows the Carnahan-Starling (C-S) Equation of State (EOS) that is given by [24]:

$$P_{Eos} = \rho RT \frac{1 + b\,\rho/4 + (b\,\rho/4)^2 - (b\,\rho/4)^3}{(1 - b\,\rho/4)^3} - a\rho^2. \tag{21}$$

where $a = 0.4963\frac{R^2T_c^2}{P_c}$, $b = 0.8727\frac{RT_c}{P_c}$, and the critical temperature is $T_c = 0.3773\frac{a}{bR}$. In the present study, we set b=4, R=1, and c=1. Also, we set a=0.5 and $T_c \approx 0.047$, the same as Li et al. [45]. The parameter a affects the interface thickness; reducing its value results in a thicker interface, leading to decreased spurious velocity and increased stability in high density ratios. For the water component, the effective mass is given by [46]:

$$\psi^1(x) = \sqrt{\frac{2(P_{EOS} - \rho c_s^2)}{G_{11}c_s^2}}. \tag{22}$$

G_{11} is set to -1, as well as for the air component, the interaction potential is equal to its density [47].

To adjust the coexistence densities and surface tension, Li et al. [45] improved the forcing term. Similarly, for the water component, the following relation is proposed for the force term [48]:

$$F^1{}_m = \begin{bmatrix} 0 \\ 6(uF_x + vF_y) + \dfrac{12\sigma|F|^2}{\psi^2\delta t(\tau_e - 0.5)} \\ -6(uF_x + vF_y) - \dfrac{12\sigma|F|^2}{\psi^2\delta t(\tau_\varsigma - 0.5)} \\ F_x \\ -F_x \\ F_y \\ -F_y \\ 2(uF_x - vF_y) \\ (uF_y + vF_x) \end{bmatrix}, \tag{23}$$

where $|F|^2 = F_x^2 + F_y^2$ and σ are used to achieve good thermodynamic consistency and to change the mechanical stability condition [48].

In the MRT LB equation, surface tension cannot be tuned independently as it is related to the density ratio. Hou et al. [49] added a source term *Eq. (25)* to the right-hand side of the MRT collision equation for a single component. In the present model, we added it to the collision MRT equation for the water component as written in the following:

$$m^{*,1} = m^1 - \Lambda[m^1(x,t) - m^{1,eq}(x,t)]| + \Delta t\left(I - \frac{\Lambda}{2}\right)F_m{}^1 + \Delta tC. \tag{24}$$

The source term in the above equation is expressed as:

$$C = \begin{bmatrix} 0 \\ 1.5\tau_e^{-1}(Q_{xx} + Q_{yy}) \\ -1.5\tau_e^{-1}(Q_{xx} + Q_{yy}) \\ 0 \\ 0 \\ 0 \\ 0 \\ -\tau_v^{-1}(Q_{xx} - Q_{yy}) \\ -\tau_v^{-1}Q_{xy} \end{bmatrix}. \tag{25}$$

The variables Q_{xx} ,Q_{yy}, and Q_{xy} are given by:

$$Q = \frac{KG_{11}}{2\psi^1(x)\sum w(|e_\alpha|^2)\left(\psi^1 \quad (x + e_\alpha) - \psi^1(x)\right) e_\alpha\, e_\alpha}. \tag{26}$$

In which the parameter K can be tuned to surface tension, with its value ranging from 0 to 1 [50]. It is important to note that in *Eq. (24)*, $m^{*,1}$ can be less than zero. Ahmed and Sung [51] employed a limiter function A_1 with a smaller τ_e^{-1} and τ_ς^{-1} in the relaxation matrix Λ_1 in order to return an MRT collision to this point again, so for component 1 the new $f^{1,*}{}_a(x,t)$ is defined as:

$$A_1 : m^{*,1}(x, t + \Delta t) \begin{cases} m^1 - \Lambda[m^1(x,t) - m^{1,eq}(x,t)]| + \Delta t\left(I - \frac{\Lambda}{2}\right) S + \Delta t C \text{iff}^{1,*}(x, t + \Delta t) \geq 0, \\ m^1 - \Lambda_1[m^1(x,t) - m^{1,eq}(x,t)]| + \Delta t\left(I - \frac{\Lambda_1}{2}\right) S + \Delta t C \qquad \text{otherwise.} \end{cases} \tag{27}$$

Subsequently, after A_1, for higher stability, limiter function A_2 is also used as a reserve, as follows:

$$A_2 : f^{1,*}(x, t + \Delta t) \begin{cases} f^{1,*}(x, t + \Delta t) \text{iff}^*(x, t + \Delta t) \geq 0, \\ \max\left(0, {}^1\!/_9 \sum_{i=0}^{8} f^{1,*}(x + e_a \Delta t, t + \Delta t)\right) \text{iff}^*(x, t + \Delta t) < 0. \end{cases} \tag{28}$$

For relaxation matrix Λ_1 we have set $\tau_e^{-1} = \tau_\varsigma^{-1} = 0.02$.

3 | Model Validation

In this section, Laplace's law for a model of the circular droplet in which a radius of $r_0 = 40$ is initially placed at the center of the domain is evaluated. Periodic boundary conditions are imposed in the x and y directions. The initial density fields are given as follows:

$$\rho(x, y) = \frac{\rho_{in} + \rho_{out}}{2} - \frac{\rho_{in} - \rho_{out}}{2} \tanh\left(\frac{2(r - r_0)}{W}\right). \tag{29}$$

In which $r = \sqrt{(x - x_c)^2 + (y - y_c)^2}$.

The center of the domain is (x_c,) yc, and W is the interface thickness and is set to 2 lattice units. ρ_{in} and ρ_{out} are the densities inside and outside the droplet, respectively.

The grid size is 200×200, and the temperature is set to $0.5T_c(T = 50^0C)$, where for water $\rho_{in(liquid)} = 0.456$ and $\rho_{out(vapor)} = 0.000055$, while for the air component, it is set to 5×10^{-7} and 0.000567 for inside and outside of the droplet.

After achieving a steady state, the pressure of the system is calculated as follows [43]:

$$P_{sys} = c_s^2 \sum_{\sigma} \rho_\sigma + \frac{1}{2} c^2 \sum_{\sigma} G_{\sigma\sigma} [\psi^\sigma(x)]^2 + \frac{1}{2} c_s^2 \sum_{\sigma \neq \bar{\sigma}} G_{\sigma\bar{\sigma}} \phi^\sigma(x)\, \phi^{\bar{\sigma}}(x). \quad (30)$$

Laplace's law gives the system pressure difference between inside and outside of the droplet, which is linearly related to the inverse of the droplet radius. For two-dimensional simulation, it is written as follows:

$$(\text{Pin} - \text{Pout}) = \frac{\gamma}{R}, \quad (31)$$

where P_{in} and P_{out} are respectively the pressure inside and outside of the droplet, γ is the surface tension, and R is the radius of the droplet.

As is seen in *Fig. 1*, for T/Tc=0.5 and the initial radius of r_0=40, the distribution of density in a 200×200 lattice domain with k= 0.68. The lack of fluctuations in the phase change region and the absence of fluctuations at the boundaries of the interface indicate the stability of the method used and its proximity to the physical one.

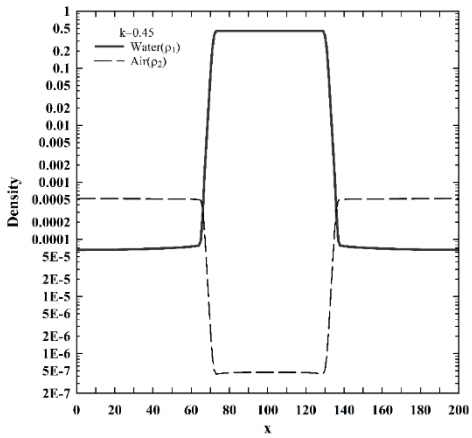

Fig. 1. distribution of liquid density for $\frac{T}{Tc} = 0.5$ and initial radius r_0=40.

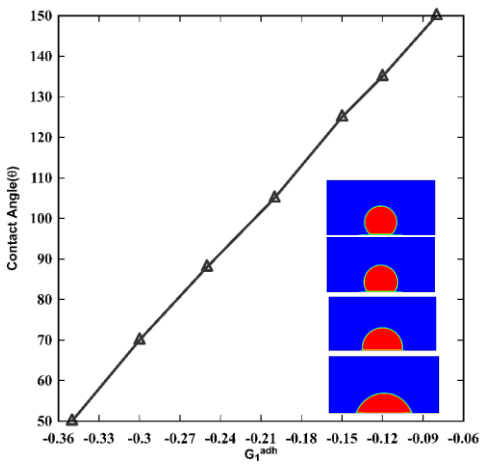

Fig. 4. Liquid droplet attached to the solid surface in different contact angles at $\frac{T}{T_c} = 0.5$.

Fig. 2 is devoted to the visualization of the results obtained by the simulation at T/T_c =0.5 with different values of k for the confirmation of Laplace's law. It is clear from the figure that there is a linear relationship between the pressure difference and the inverse of the droplet radius. From the results, it is observed that by changing the value of k, the surface tension could be varied independently of the density ratio. For this study, we take k=0.68.

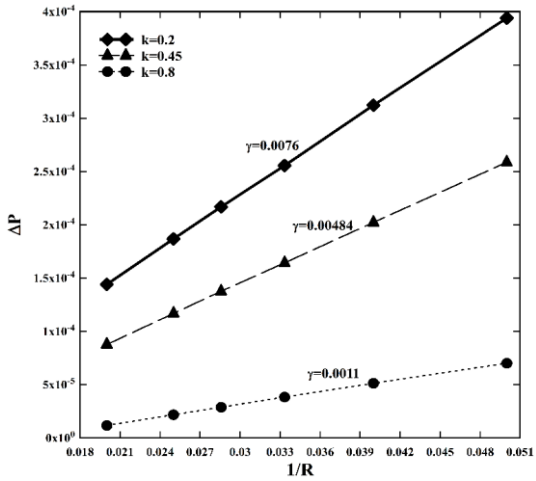

Fig. 2. Pressure difference and inverse of droplet radius for validation of Laplace's law with different values of k at $T/Tc = 0.5$.

Fig. 3 shows the pressure distribution in the x direction of the computational domain for different values of k. It is clear from the figure that the pressure fluctuations near the vapor-liquid interface happen due to a sharp variation of density, which is ignored in the calculation of ΔP.

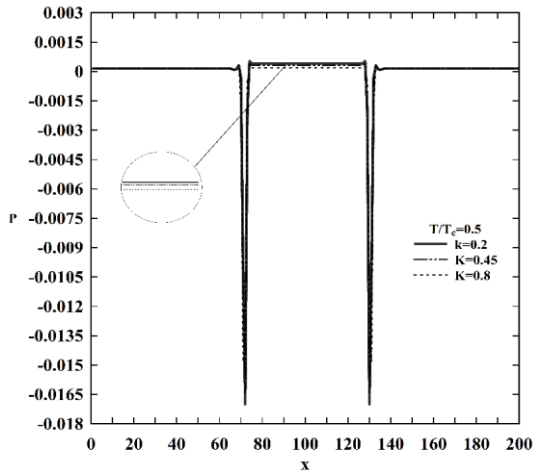

Fig. 3. Pressure distribution along the x direction at $T/Tc = 0.5$.

The contact angle characterizes the wettability of the surface. In fact, if the contact angle is less than 900, then the surface is hydrophilic, and the liquid phase expands like a film on the solid surface. On the other hand, if the contact angle is more than 900, then the surface is non-wetting or hydrophobic, and the liquid phase is formed like a droplet on the solid surface.

In the simulations, the computational domain is 200 × 100. Periodic boundary conditions have been applied on the left and right edges. Bounce-back boundary conditions have been employed on the bottom and top solid surfaces. After convergence of the simulation, the contact angle has been evaluated according to the following expression:

$$\theta = \begin{cases} \arcsin\left(\frac{b}{2r}\right) \theta \leq 90^0, \\ \pi - \arcsin\left(\frac{b}{2r}\right) \theta > 90^0, \end{cases} \tag{32}$$

where r is defined as:

$$r = \frac{4h^2 + b^2}{8h}, \tag{33}$$

where h and b are the height and the base length of the droplet on the surface, respectively. *Fig. 4* is about liquid droplets in different contact angles on a solid wall, indicating an almost linear relationship between the adhesion factor and the contact angle.

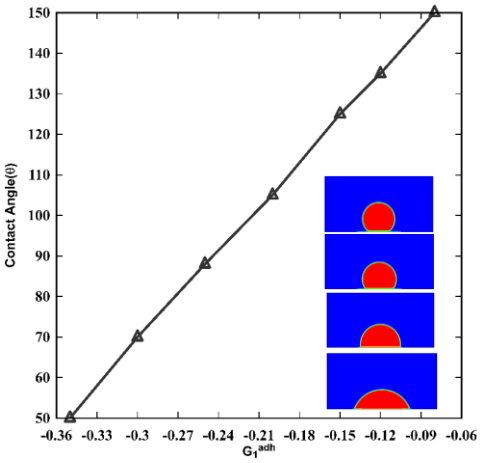

Fig. 4. Liquid droplet attached to the solid surface in different contact angles at $\frac{T}{T_c} = 0.5$.

3.1 | Single-Phase Permeability Calculation

One of the parameters in order to study the flow in the porous media is the resistance to flow, which is the permeability. According to Darcy's law, the permeability K of the porous medium is estimated using the following equation:

$$K = \frac{\mu U}{\Delta P}, \tag{34}$$

where U is the volume-averaged flow velocity, μ is the dynamic viscosity of the fluid, and ΔP denotes the pressure gradient. Darcy's law is applicable to porous media flows with low Reynolds number and negligible convection effects [52]. It should be noted that the Reynolds number based on the fiber diameter for the liquid water and air flows in the PTLs is lower than 0.1 in the current work; therefore, the Darcy equation is applicable. The Gebart correlation has been extensively used in theoretical, numerical, and experimental studies to estimate the flow permeability of ordered arrays of fibers. In the case of porous media with a porosity of ε and a mean particle radius of R, the Gebart relation in the limit of closely packed fibers provides the estimation of the flow permeability K, which is as follows:

$$\frac{K}{R^2} = C_g \left[\sqrt{\frac{1-\varepsilon_c}{1-\varepsilon}} - 1 \right]^{2.5}, \tag{35}$$

where εc is the critical porosity below which flow cannot happen (i.e., percolation threshold). Cg is the proportionality constant, which is also called the geometric factor. For a square arrangement $C_g = \frac{16}{9\pi\sqrt{2}}$ and

$$\varepsilon_c = 1 - \pi/4. \tag{36}$$

Tamayol and Bahrami (TB) have used the scaling analysis to find the following relation for the permeability of a fibrous medium and its microstructure and geometric parameters, including tortuosity, pore diameter, and porosity.

$$\frac{K}{R^2} = 0.048(1-\varphi)\left[\left(\frac{\pi}{4\varphi}\right)^2 - \frac{\pi}{2\varphi} + 1\right]\left[1 + 0.72\frac{\varphi}{(0.89-\varphi)^{0.54}}\right], \quad (36)$$

where φ represents the solids volume fraction, i.e φ=1-ε. *Table 1* shows the values of the flow permeability from the LBM results in comparison with Gebart's correlation and TB results, where the fiber radii range between 5 and 15 μm and the porosity varies from 0.65 to 0.85, which is common for the GDL in the PEMFC. It has been determined that there is a good agreement between the permeability-porosity relationship from the LBM and Gebart's or TB's analytical solutions.

Table 1. Flow permeability, K/R^2, in the GDL.

Prosity	Flow Permeability, K/R^2, in the GDL				
ε	LBM	Gebart	Difference	TB	Difference
0.65	6.692×10^{-2}	6.9905×10^{-2}	0.5%	6.5153×10^{-2}	6.8%
0.75	0.1702	0.20779	18.11%	0.20088	15.29%
0.85	0.773	0.746	3.75%	0.8155	5.11%

4 | Results and Discussion

A standard PEMFC electrode utilizing the interdigitated gas distributor as designed by Nguyen [8] is depicted in *Fig. 5*. According to *Fig. 5a*, air enters the multilayer hydrophobic PTLs (GDL and MPL) and is directed through the lands into the outlet channel fingers. In *Fig. 5b*, the computational domain used within the present study is illustrated. This domain encompasses half the inlet channel, half the outlet channel, one land, and PTFL. The CL is taken to function like an extremely thin interface attached to the bottom of the PTLs.

In *Fig. 5b*, the GDL (region "A") layer is formed by randomly positioning circular solids of average diameter 16 μm in the layer with thickness 150 μm. The porosity of the GDL layer is approximately equal to 0.8 prior to analyzing the PLTs, and its contact angle is taken to be 115-135 degrees. After that, an MPL layer with a thickness of 25-70 μm (region "B") is created through the random positioning of square particles (4 μm edge length). MPL averages 0.76 with respect to porosity, whereas its contact angle equals 150 degrees.

The standard PEMFC electrode having the structure of an interdigitated gas distributor as invented by Nguyen [8] is shown in *Fig. 5*. From *Fig. 5a*, it can be seen that air is fed into the multilayer hydrophobic PTLs (GDL and MPL) and is carried via the lands into the outlet channel fingers. In *Fig. 5b*, the computational domain utilized in the current study is shown. The computational domain includes half the inlet channel, half the outlet channel, one land, and PTFL. It is considered that the CL acts like a very thin interface connected to the bottom of the PTLs.

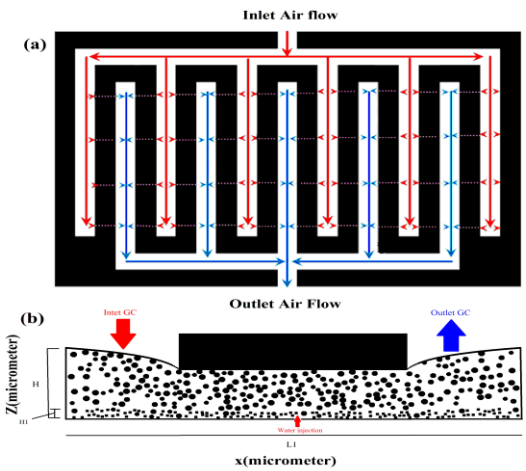

Fig. 5. A typical PEMFC electrode with interdigitated gas distributor.

In *Fig. 5b*, the GDL (region "A") layer is generated by random placement of circles having an average diameter of 16 μm in a layer having a thickness of 150 μm. The porosity of the GDL layer is about 0.8 before analysis of the PLTs, and its contact angle is 115-135 degrees. Then the MPL layer, having a thickness of 25-70 μm (region "B"), is generated by random placement of square solids having an edge length of 4 μm. MPL has a porosity of about 0.76, and its contact angle is 150 degrees. The values of the parameters used in the computational domain are given in *Table 2*.

Table 2. Geometry parameters.

Parameters	Value
Dimensions of the computational domain	
Width of the inlet/outlet channel	500 μm
Width of the land	500 μm
Height of the PTL(H)	200 μm
Height of the MPL(H1)	35-70 μm
Operating conditions	
Velocity of air inlet to PTFL	V=0.5-1 m/s
Operation temperature	T=323K
Outlet pressure of GC	1 atm
Capillary number of liquid water inlet	

The location of liquid-water injection into the PTLs is a critical parameter governing water management in PEMFCs. The injection location directly affects the liquid-water transport pathway, its accumulation within the porous structure, the spatial distribution of water saturation, and the time required for the system to reach a quasi-steady state.

In general, when liquid water is generated or injected at a location farther from the outlet, it must travel a longer distance through the porous media before being removed. This extended transport pathway promotes liquid-water accumulation within the PTLs, resulting in higher water saturation and an increased risk of flooding.

In the present study, the Effect of the liquid-water injection location on water transport through the PTLs was investigated under identical operating and structural conditions. The compression ratio was set to 85%, the capillary number was Ca = 0.0004, and the MPL thickness was 70 μm. The initial porosities of the GDL and MPL were set to 82% and 79%, respectively, while the inlet air velocity was maintained at 3 m/s. Five water injection points with an average diameter of approximately 5 μm were considered at different locations within the computational domain.

Based on their relative positions with respect to the gas inlet, rib, and outlet, three representative injection configurations were examined: 1) injection beneath the gas inlet region, 2) injection in the middle region beneath the rib, and 3) injection beneath the gas outlet region. The corresponding injection locations are summarized in *Table 3*.

Table 3. Different liquid-water injection locations considered in the simulations.

Configuration	Water Injection Location
1	Beneath the gas inlet region
2	In the middle region beneath the rib
3	Beneath the gas outlet region

4.1 | Temporal Evolution of Water Saturation

The temporal progression of the water saturation distribution in the PTLs under investigation is shown in *Figs. 6-8* for each water injection location. As illustrated in *Fig. 6*, in the case of liquid water injection below the gas inlet zone (Configuration 1), liquid water needs to move through a long drainage distance prior to reaching the outlet. In the early stage of simulation, liquid water mainly resides in the region around the water

injection area. With progressing time, liquid water moves forward through the PTLs up to the outlet point, causing expansion of the saturated water region.

Configuration 1 features a relatively long drainage distance, which results in more water accumulation inside the porous structure and hence in high water saturation. Additionally, increased drainage distance causes more time needed to remove liquid water from the computational domain. This configuration features a relatively long transient process until the quasi-steady state is reached. Liquid water accumulation can impede the mass transfer of reactant gases into the catalyst layer due to partial blocking of gas pathways inside the PTLs.

With the movement of the injection site to the middle region under the rib (Configuration 2), the effective distance between the water injection point and the outlet becomes shorter. As a result, the movement of the liquid water to the outlet becomes easier in Comparison 2 than in Comparison 1. The smaller drainage distance leads to a lower liquid-water accumulation in the upstream region of the PTLs and an improved spatial distribution of water saturation.

Nevertheless, there is a significant accumulation of liquid water in the central region of the PTLs. This fact shows that despite the improvement in liquid-water removal caused by the movement of the injection site toward the outlet, the liquid-water removal process is affected by the complicated interplay between capillary and viscous forces and gas-phase movement through the porous medium.

The best water distribution is achieved in Configuration 3, where liquid water is injected in the area near the outlet point (*Fig. 8*). In this comparison, the shortest transport path for the liquid water is observed before the movement to the outlet point.

As a result, water is removed from the PTLs faster than in Configurations 1 and 2. An important observation is that no significant liquid-water accumulation occurs beneath the rib or in the gas inlet region in Configuration 3. This behavior is particularly advantageous for PEMFC water management because the gas transport pathways remain relatively unobstructed. Consequently, reactant-gas transport through the PTLs can be facilitated, while the risk of local flooding is reduced. These characteristics are expected to contribute to improved mass transport and, consequently, enhanced PEMFC performance.

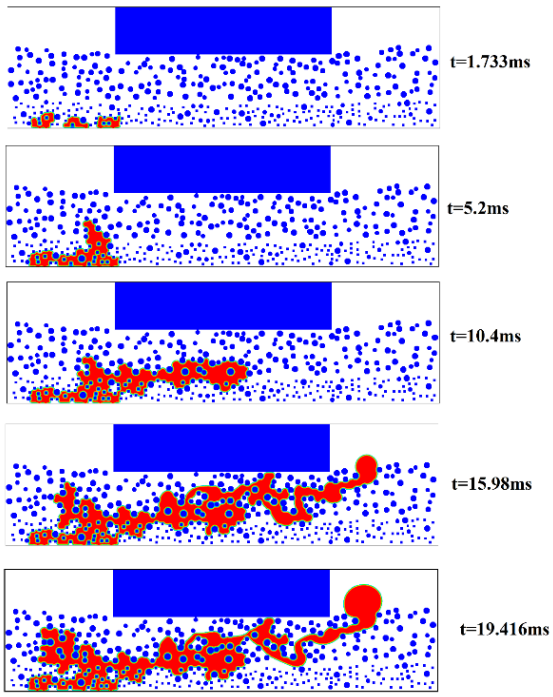

Fig. 6. Water saturation distribution within the PTLs for water injection beneath the gas inlet region at a compression ratio of 85%, T=50 °C, MPL=70 μm, V_{air}=3 m/s, and Ca = 0.0004.

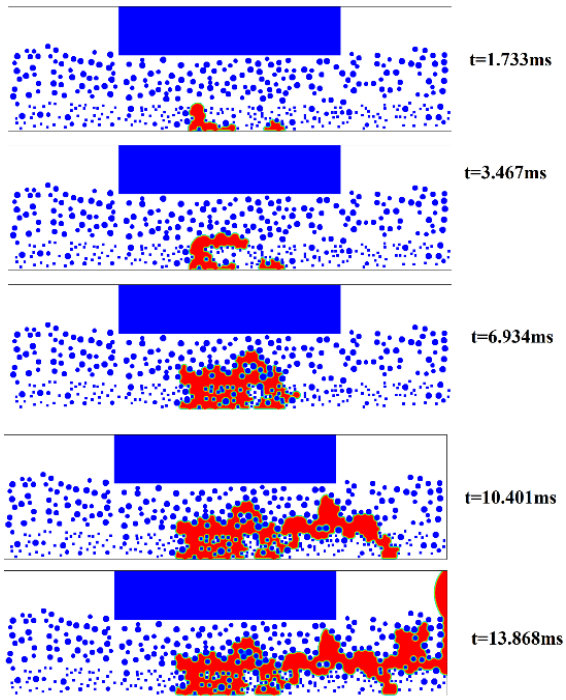

Fig. 7. Water saturation distribution within the PTLs for water injection in the middle region of the computational domain at a compression ratio of 85%, T=50 °C, MPL=70 μm, V_{air}=3 m/s, and Ca = 0.0004.

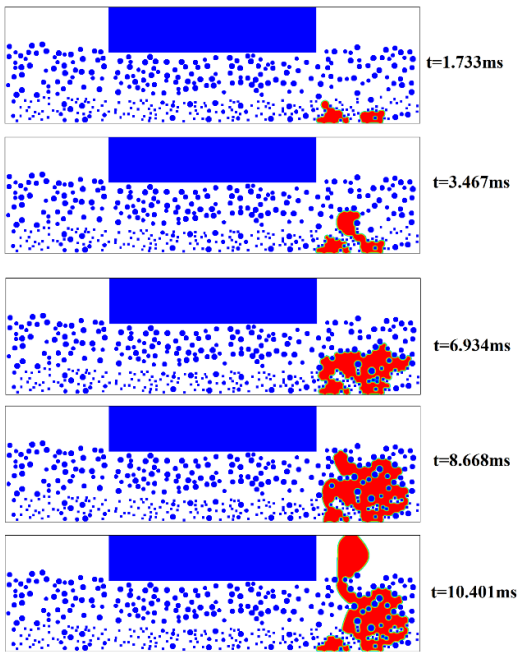

Fig. 8. Water saturation distribution within the PTLs for water injection beneath the liquid-water outlet region at a compression ratio of 85%, T=50 °C, MPL=70μm, V_{air}=3 m/s, and Ca = 0.0004.

The analysis of the differences between the water saturations achieved in each of the three injections proves the considerable effect of injection point on liquid water accumulation in PTLs. As seen in *Figs. 9- 11*, the maximal water saturation in Configuration 1(*Fig. 9*) is almost twice as high as in Configuration 3 (*Fig. 11*), which can be explained by the longer drainage path corresponding to the inlet point of injection. Configuration 2 (*Fig. 10*) is characterized by the intermediate water distribution behavior between

Configurations 1 and 3. The decrease in water saturation corresponds to the movement of liquid water out of the injection area towards the outlet. In comparison with Configuration 1, the decreased distance of transportation of liquid water contributes to water removal and less accumulation in the PTLs.

At last, Configuration 3 shows the highest efficiency in liquid water removal among all considered cases. The nearness of the injection point to the outlet decreases the residence time of liquid water in the PTLs and, consequently, prevents the appearance of highly water-saturated areas. Thus, it is obvious that shifting the injection point towards the outlet helps to prevent the accumulation of water.

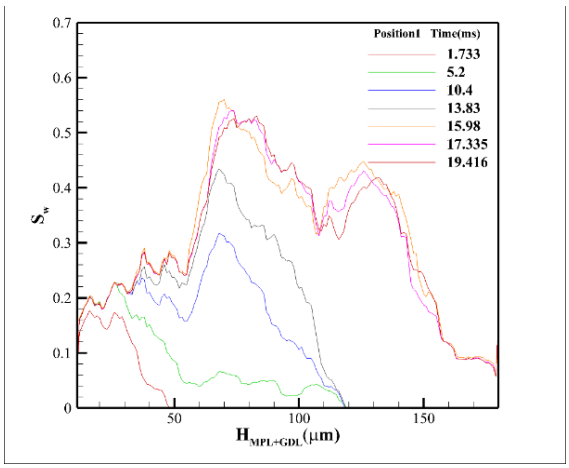

Fig. 9. Temporal evolution of water saturation distribution within the PTLs for liquid-water injection in the middle region beneath the rib at a compression ratio of 85%, Ca = 0.0004, MPL thickness of 70 μm, and inlet air velocity of 3 m/s.

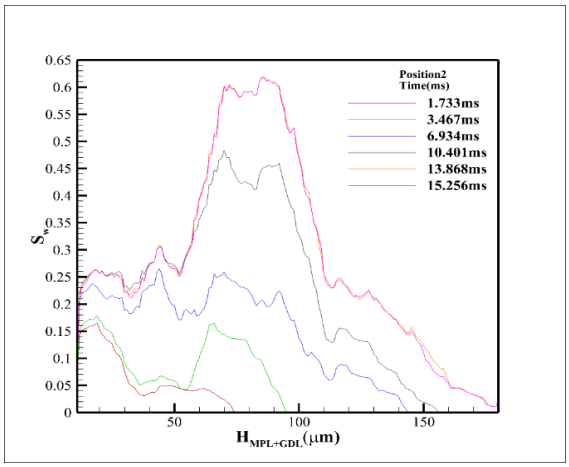

Fig. 10. Temporal evolution of water saturation distribution within the PTLs for liquid-water injection beneath the gas outlet region at a compression ratio of 85%, Ca = 0.0004, MPL thickness of 70 μm, and inlet air velocity of 3 m/s.

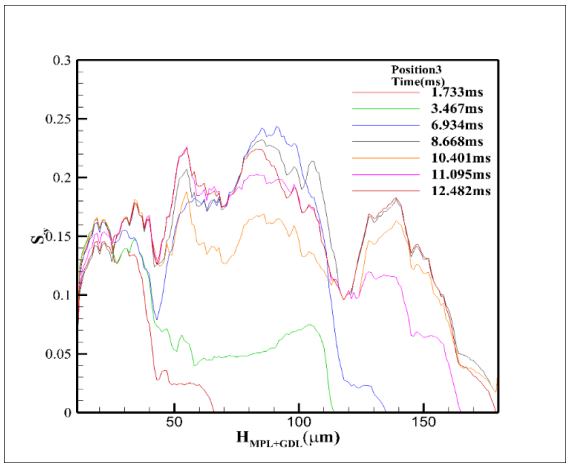

Fig. 11. Comparison of the temporal evolution of average water saturation within the PTLs for different liquid-water injection locations at a compression ratio of 85%, Ca = 0.0004, MPL thickness of 70 μm, and inlet air velocity of 3 m/s.

Fig. 12 displays the time behavior of the average water saturation of the PTLs for the three water injection locations. In the first stage, the average water saturation rises steadily for the three configurations, which means that the liquid water gradually builds up and propagates through the PTLs. Despite the relatively similar behaviors of the three configurations in the beginning, their behaviors differ significantly in the course of the development of the liquid-water distribution.

For *Position 1*, where water is injected under the gas inlet, the average water saturation keeps rising to a quasi-steady level of 0.34–0.35 until around 15 ms. This is due to the relatively long drainage path for the liquid water to the outlet. As a result, the liquid water stays in the PTLs for a longer time, resulting in higher average water saturation.

In *Position 2*, where water is injected in the middle region under the rib, the average water saturation initially shows a trend somewhat resembling *Position 1*. After around 12 ms, however, the saturation starts leveling down and stabilizes at around 0.26. When compared to *Position 1*, a lower steady-state water saturation suggests that moving the injection point closer to the middle of the computational domain increases the efficiency of liquid-water elimination and minimizes the accumulation of liquid within the PTLs.

Position 3, characterized by water injection under the liquid-water outlet, demonstrates the lowest average water saturation. In this position, the average water saturation attains values within the range of 0.12-0.15 after the transient period and then shows oscillations. These oscillations arise due to the shorter drainage path from the point of injection to the outlet, ensuring that liquid water is removed from the PTLs faster. As a consequence, the amount of liquid water accumulation within the porous matrix is much lower than in *Positions 1* and *2*.

Under quasi-steady conditions, the average water saturation for *Position 3* is approximately 57–65% lower than that for *Position 1* and approximately 42–54% lower than that for *Position 2*, based on the representative saturation values obtained from the plotted results. In contrast, *Position 2* exhibits an average water saturation approximately 23–26% lower than *Position 1*. These results clearly demonstrate that moving the water injection location toward the outlet substantially enhances liquid-water removal and suppresses water accumulation within the PTLs.

The oscillatory behavior observed for *Position 3* may be associated with the intermittent detachment and removal of liquid-water clusters near the outlet. As water accumulates locally, capillary forces promote the formation of liquid clusters, which are subsequently transported and discharged through the outlet. This dynamic process results in temporal fluctuations in the spatially averaged water saturation. Nevertheless, the overall saturation level remains considerably lower than those obtained for *Positions 1* and *2*.

The average water saturation of *Position 3* is roughly 57-65% and 42-54% lower compared to *Position 1* and *Position 2*, respectively, by taking into account the representative water saturations for each position according to the graph results. However, for *Position 2*, the average water saturation is about 23-26% less than that of *Position 1*. Such results show clearly that the relocation of the water injection point towards the outlet improves the removal of liquid water and minimizes its accumulation in the PTLs.

The oscillations recorded at *Position 3* can be related to the occasional removal of liquid-water clusters near the outlet. Indeed, as water collects locally due to the accumulation process, capillary forces cause the formation of water clusters, which are then carried out of the domain through the outlet. This phenomenon leads to the temporal variations in the water saturation averaged spatially. But in any case, the average water saturation is still relatively low compared to *Positions 1* and *2*.

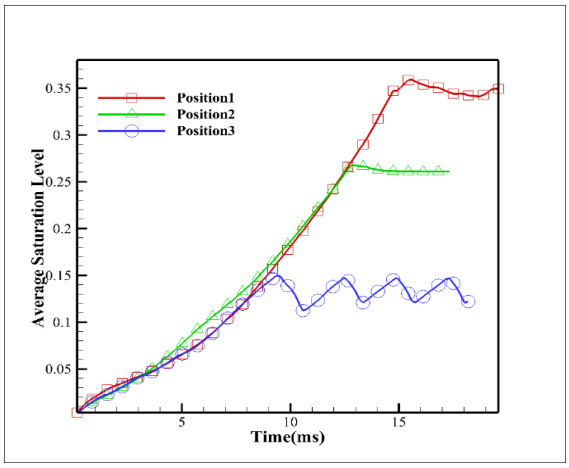

Fig. 12. Temporal evolution of the average water saturation within the PTLs for different liquid-water injection locations at a compression ratio of 85%, T = 50, MPL thickness of 70 μm, inlet air velocity of 3 m/s, and Ca = 0.0004.

5 | Conclusion

In this study, a pore-scale multiphase MRT-LBM model was developed to investigate liquid-water transport and accumulation within the PTLs of an interdigitated PEMFC. The model was validated against Laplace's law, droplet contact-angle behavior, and permeability correlations, showing good agreement with analytical and empirical results. The simulations demonstrated that the liquid-water injection location strongly affects water accumulation and drainage within the PTLs. Injection beneath the gas inlet resulted in the highest average water saturation (approximately 0.34–0.35), whereas injection beneath the outlet produced the lowest values (approximately 0.12–0.15). The outlet-side injection configuration reduced the average water saturation by approximately 57–65% compared with the inlet-side configuration and by 42–54% compared with the middle-region configuration.

Overall, positioning the liquid-water injection location closer to the outlet promotes more efficient water removal, reduces water accumulation, and helps maintain open gas transport pathways within the PTLs. The developed pore-scale MRT-LBM framework provides a useful tool for analyzing multiphase transport and optimizing water management in PEMFCs.

Conflict of Interest

The authors declare that there are no conflicts of interest regarding the publication of this paper.

Data Availability

The datasets generated and/or analyzed during the current study are included in this article.

Funding

This study was carried out without any specific funding from public, commercial, or non-profit organizations.

References

[1] Shojaeefard, M. H., Molaeimanesh, G. R., Nazemian, M., & Moqaddari, M. R. (2016). A review on microstructure reconstruction of PEM fuel cells porous electrodes for pore scale simulation. *International journal of hydrogen energy*, *41*(44), 20276–20293. https://doi.org/10.1016/j.ijhydene.2016.08.179

[2] Springer, T. E., Zawodzinski, T. A., & Gottesfeld, S. (1991). Polymer electrolyte fuel cell model. *Journal of the electrochemical society*, *138*(8), 2334. https://doi.org/10.1149/1.2085971

[3] Li, H., Tang, Y., Wang, Z., Shi, Z., Wu, S., Song, D., …& Mazza, A. (2008). A review of water flooding issues in the proton exchange membrane fuel cell. *Journal of power sources*, *178*(1), 103–117. https://doi.org/10.1016/j.jpowsour.2007.12.068

[4] Dicks, A., & Rand, D. A. J. (2018). *Fuel cell systems explained*. Wiley Online Library. https://doi.org/10.1002/9781118706992.fmatter

[5] Molaeimanesh, G. R., Saeidi Googarchin, H., & Qasemian Moqaddam, A. (2016). Lattice Boltzmann simulation of proton exchange membrane fuel cells – A review on opportunities and challenges. *International journal of hydrogen energy*, *41*(47), 22221–22245. https://doi.org/10.1016/j.ijhydene.2016.09.211

[6] Tüber, K., Pócza, D., & Hebling, C. (2003). Visualization of water buildup in the cathode of a transparent PEM fuel cell. *Journal of power sources*, *124*(2), 403–414. https://doi.org/10.1016/S0378-7753(03)00797-3

[7] Baschuk, J. J., & Li, X. (2000). Modelling of polymer electrolyte membrane fuel cells with variable degrees of water flooding. *Journal of power sources*, *86*(1), 181–196. https://doi.org/10.1016/S0378-7753(99)00426-7

[8] Nguyen, T. V. (1996). A gas distributor design for proton-exchange-membrane fuel cells. *Journal of the electrochemical society*, *143*(5), L103. https://doi.org/10.1149/1.1836666

[9] Wood, D. L., Yi, J. S., & Nguyen, T. V. (1998). Effect of direct liquid water injection and interdigitated flow field on the performance of proton exchange membrane fuel cells. *Electrochimica acta*, *43*(24), 3795–3809. https://doi.org/10.1016/S0013-4686(98)00139-X

[10] Kazim, A., Liu, H. T., & Forges, P. (1999). Modelling of performance of PEM fuel cells with conventional and interdigitated flow fields. *Journal of applied electrochemistry*, *29*(12), 1409–1416. https://doi.org/10.1023/A:1003867012551

[11] Hu, M., Zhu, X., Wang, M., Gu, A., & Yu, L. (2004). Three dimensional, two phase flow mathematical model for PEM fuel cell: Part II. Analysis and discussion of the internal transport mechanisms. *Energy conversion and management*, *45*(11), 1883–1916. https://doi.org/10.1016/j.enconman.2003.09.023

[12] Hu, M., Gu, A., Wang, M., Zhu, X., & Yu, L. (2004). Three dimensional, two phase flow mathematical model for PEM fuel cell: Part I. Model development. *Energy conversion and management*, *45*(11), 1861–1882. https://doi.org/10.1016/j.enconman.2003.09.022

[13] Hu, G., Fan, J., Chen, S., Liu, Y., & Cen, K. (2004). Three-dimensional numerical analysis of proton exchange membrane fuel cells (PEMFCs) with conventional and interdigitated flow fields. *Journal of power sources*, *136*(1), 1–9. https://doi.org/10.1016/j.jpowsour.2004.05.010

[14] Su, Z. Y., Liu, C. T., Chang, H. P., Li, C. H., Huang, K. J., & Sui, P. C. (2008). A numerical investigation of the effects of compression force on PEM fuel cell performance. *Journal of power sources*, *183*(1), 182–192. https://doi.org/10.1016/j.jpowsour.2008.04.060

[15] Shi, Z., & Wang, X. (2008). A numerical study of flow crossover between adjacent flow channels in a proton exchange membrane fuel cell with serpentine flow field. *Journal of power sources*, *185*(2), 985–992. https://doi.org/10.1016/j.jpowsour.2008.09.008

[16] Lin, J. H., Chen, W. H., Su, Y. J., & Ko, T. H. (2008). Effect of gas diffusion layer compression on the performance in a proton exchange membrane fuel cell. *Fuel*, *87*(12), 2420–2424. https://doi.org/10.1016/j.fuel.2008.03.001

[17] Chippar, P., O, K., Kang, K., & Ju, H. (2012). A numerical investigation of the effects of GDL compression and intrusion in polymer electrolyte fuel cells (PEFCs). *International journal of hydrogen energy*, *37*(7), 6326–6338. https://doi.org/10.1016/j.ijhydene.2011.04.154

[18] Molaeimanesh, G. R., & Nazemian, M. (2017). Investigation of GDL compression effects on the performance of a PEM fuel cell cathode by lattice Boltzmann method. *Journal of power sources*, *359*, 494–506. https://doi.org/10.1016/j.jpowsour.2017.05.078

[19] Mahmoudi, A. H., Ramiar, A., & Esmaili, Q. (2016). Effect of inhomogeneous compression of gas diffusion layer on the performance of PEMFC with interdigitated flow field. *Energy conversion and management*, *110*, 78–89. https://doi.org/10.1016/j.enconman.2015.12.012

[20] Shi, Z., Wang, X., & Guessous, L. (2010). Effect of compression on the water management of a proton exchange membrane fuel cell with different gas diffusion layers. *Journal of fuel cell science and technology*, *7*(2), 21012. https://doi.org/10.1115/1.3177451

[21] Ihonen, J., Mikkola, M., & Lindbergh, G. (2004). Flooding of gas diffusion backing in PEFCs : Physical and electrochemical characterization. *Journal of the electrochemical society*, *151*(8), A1152. https://doi.org/10.1149/1.1763138

[22] Nam, J. H., & Kaviany, M. (2003). Effective diffusivity and water-saturation distribution in single- and two-layer PEMFC diffusion medium. *International journal of heat and mass transfer*, *46*(24), 4595–4611. https://doi.org/10.1016/S0017-9310(03)00305-3

[23] Zhang, F. Y., Yang, X. G., & Wang, C. Y. (2005). Liquid water removal from a polymer electrolyte fuel cell. *Journal of the electrochemical society*, *153*(2), A225. https://doi.org/10.1149/1.2138675

[24] Chen, L., Kang, Q., Tang, Q., Robinson, B. A., He, Y. L., & Tao, W. Q. (2015). Pore-scale simulation of multicomponent multiphase reactive transport with dissolution and precipitation. *International journal of heat and mass transfer*, *85*, 935–949. https://doi.org/10.1016/j.ijheatmasstransfer.2015.02.035

[25] Molaeimanesh, G. R., & Akbari, M. H. (2015). A pore-scale model for the cathode electrode of a proton exchange membrane fuel cell by lattice Boltzmann method. *Korean journal of chemical engineering*, *32*(3), 397–405. https://doi.org/10.1007/s11814-014-0229-6

[26] Niu, X. D., Munekata, T., Hyodo, S. A., & Suga, K. (2007). An investigation of water-gas transport processes in the gas-diffusion-layer of a PEM fuel cell by a multiphase multiple-relaxation-time lattice Boltzmann model. *Journal of power sources*, *172*(2), 542–552. https://doi.org/10.1016/j.jpowsour.2007.05.081

[27] Park, J., Matsubara, M., & Li, X. (2007). Application of lattice Boltzmann method to a micro-scale flow simulation in the porous electrode of a PEM fuel cell. *Journal of power sources*, *173*(1), 404–414. https://doi.org/10.1016/j.jpowsour.2007.04.021

[28] Park, J., & Li, X. (2008). Multi-phase micro-scale flow simulation in the electrodes of a PEM fuel cell by lattice Boltzmann method. *Journal of power sources*, *178*(1), 248–257. https://doi.org/10.1016/j.jpowsour.2007.12.008

[29] Mukherjee, P. P., Wang, C. Y., & Kang, Q. (2009). Mesoscopic modeling of two-phase behavior and flooding phenomena in polymer electrolyte fuel cells. *Electrochimica acta*, *54*(27), 6861–6875. https://doi.org/10.1016/j.electacta.2009.06.066

[30] Kim, K. N., Kang, J. H., Lee, S. G., Nam, J. H., & Kim, C. J. (2015). Lattice Boltzmann simulation of liquid water transport in microporous and gas diffusion layers of polymer electrolyte membrane fuel cells. *Journal of power sources*, *278*, 703–717. https://doi.org/10.1016/j.jpowsour.2014.12.044

[31] Hao, L., & Cheng, P. (2009). Lattice Boltzmann simulations of anisotropic permeabilities in carbon paper gas diffusion layers. *Journal of power sources*, *186*(1), 104–114. https://doi.org/10.1016/j.jpowsour.2008.09.086

[32] Chen, L., Luan, H. B., He, Y. L., & Tao, W. Q. (2012). Pore-scale flow and mass transport in gas diffusion layer of proton exchange membrane fuel cell with interdigitated flow fields. *International journal of thermal sciences*, *51*, 132–144. https://doi.org/10.1016/j.ijthermalsci.2011.08.003

[33] Shojaeefard, M. H., Molaeimanesh, G. R., & Moqaddari, M. R. (2019). Effects of compression on the removal of water droplet from GDLs of PEM fuel cells. *Fuel cells*, *19*(6), 675–684. https://doi.org/10.1002/fuce.201900101

[34] Deng, H., Hou, Y., & Jiao, K. (2019). Lattice Boltzmann simulation of liquid water transport inside and at interface of gas diffusion and micro-porous layers of PEM fuel cells. *International journal of heat and mass transfer*, *140*, 1074–1090. https://doi.org/10.1016/j.ijheatmasstransfer.2019.05.097

[35] Zhu, W., Wang, M., & Chen, H. (2017). Study on multicomponent pseudo-potential model with large density ratio and heat transfer. *International communications in heat and mass transfer*, *87*, 183–191. https://doi.org/10.1016/j.icheatmasstransfer.2017.07.007

[36] Li, Q., Luo, K. H., & Li, X. J. (2013). Lattice Boltzmann modeling of multiphase flows at large density ratio with an improved pseudopotential model. *Physical review e—statistical, nonlinear, and soft matter physics*, *87*(5), 53301. https://doi.org/10.1103/PhysRevE.87.053301

[37] Yu, Z., & Fan, L. S. (2010). Multirelaxation-time interaction-potential-based lattice Boltzmann model for two-phase flow. *Physical review e*, *82*(4), 46708. ttps://doi.org/10.1103/PhysRevE.82.046708

[38] Guo, Z., & Zheng, C. (2008). Analysis of lattice Boltzmann equation for microscale gas flows: Relaxation times, boundary conditions and the Knudsen layer. *International journal of computational fluid dynamics*, *22*(7), 465–473. https://doi.org/10.1080/10618560802253100

[39] Zheng, L., Shi, B., & Guo, Z. (2008). Multiple-relaxation-time model for the correct thermohydrodynamic equations. *Physical review e*, *78*(2), 26705. https://doi.org/10.1103/PhysRevE.78.026705

[40] Sega, M., M., Sbragaglia, S. S., Kantorovich, & Ivanov, A. O. (2013). Mesoscale structures at complex fluid–fluid interfaces: A novel lattice Boltzmann/molecular dynamics coupling. *Soft matter*, *9*(42), 10092–10107. https://doi.org/10.1039/C3SM51556G

[41] Sbragaglia, M., Benzi, R., Biferale, L., Succi, S., Sugiyama, K., & Toschi, F. (2007). Generalized lattice Boltzmann method with multirange pseudopotential. *Physical review e*, *75*(2), 26702. https://doi.org/10.1103/PhysRevE.75.026702

[42] Yang, Q., He, X., & Peng, H. (2024). Lattice Boltzmann modelling of multicomponent and multiphase flow with high density ratio. *European journal of mechanics - b/fluids*, *105*, 14–24. https://doi.org/10.1016/j.euromechflu.2023.12.014

[43] Liu, M., Yu, Z., Wang, T., Wang, J., & Fan, L.-S. (2010). A modified pseudopotential for a lattice Boltzmann simulation of bubbly flow. *Chemical engineering science*, *65*(20), 5615–5623. 10.1016/j.ces.2010.08.014

[44] Shan, X. (2006). Analysis and reduction of the spurious current in a class of multiphase lattice Boltzmann models. *Phys. rev. e*, *73*(4), 47701. https://doi.org/10.1103/PhysRevE.73.047701

[45] Yu, Z. (2009). *A novel lattice Boltzmann method for direct numerical simulation of multiphase flows*. The Ohio State University. https://dissertation.com/abstract/1842713

[46] Yuan, P., & Schaefer, L. (2006). Equations of state in a lattice Boltzmann model. *Physics of fluids*, *18*(4), 42101. https://doi.org/10.1063/1.2187070

[47] Hu, A., Li, L., Chen, S., Liao, Q., & Zeng, J. (2013). On equations of state in pseudo-potential multiphase lattice Boltzmann model with large density ratio. *International journal of heat and mass transfer*, *67*, 159–163. https://doi.org/10.1016/j.ijheatmasstransfer.2013.08.005

[48] Sbragaglia, M., & Belardinelli, D. (2013). Interaction pressure tensor for a class of multicomponent lattice Boltzmann models. *Physical review E*, *88*(1), 13306. https://doi.org/10.1103/PhysRevE.88.013306

[49] Hou, Y., Deng, H., Du, Q., & Jiao, K. (2018). Multi-component multi-phase lattice Boltzmann modeling of droplet coalescence in flow channel of fuel cell. *Journal of power sources*, *393*, 83–91. https://doi.org/10.1016/j.jpowsour.2018.05.008

[50] Li, Q., Luo, K. H., Kang, Q. J., He, Y. L., Chen, Q., & Liu, Q. (2016). Lattice Boltzmann methods for multiphase flow and phase-change heat transfer. *Progress in energy and combustion science*, *52*, 62–105. https://doi.org/10.1016/j.pecs.2015.10.001

[51] Ahmed, D. H., & Sung, H. J. (2006). Effects of channel geometrical configuration and shoulder width on PEMFC performance at high current density. *Journal of power sources*, *162*(1), 327–339. https://doi.org/10.1016/j.jpowsour.2006.06.083

[52] Wu, Y., Gui, N., Yang, X., Tu, J., & Jiang, S. (2018). Improved stability strategies for pseudo-potential models of lattice Boltzmann simulation of multiphase flow. *International journal of heat and mass transfer*, *125*, 66–81. https://doi.org/10.1016/j.ijheatmasstransfer.2018.04.021